Journal of Nuclear Medicine, published on April 9, 2015 as doi:10.2967/jnumed.115.154807

Clinical assessment of emission- and segmentation-based MR-guided attenuation correction in whole-body time-of-flight PET/MRI

Abolfazl Mehranian[1] and Habib Zaidi[1,2,3†]

[1]Division of Nuclear Medicine and Molecular Imaging, Geneva University Hospital, Geneva, Switzerland
[2]Geneva Neuroscience Centre, University of Geneva, Geneva, Switzerland
[3]Department of Nuclear Medicine and Molecular Imaging, University of Groningen, Groningen, Netherlands

[†]**Corresponding author:**

Habib Zaidi, Ph.D
Geneva University Hospital
Division of Nuclear Medicine and Molecular Imaging
CH-1211 Geneva, Switzerland
Tel: +41 22 372 7258
Fax: +41 22 372 7169
email: habib.zaidi@hcuge.ch

Short title: Comparison of emission- and segmentation-based attenuation correction in PET/MRI

Words count

Abstract: ~250

Total manuscript: ~5620

ABSTRACT

The joint maximum likelihood reconstruction of activity and attenuation (MLAA) for emission-based attenuation correction has regained attention since the advent of time-of-flight PET/MRI. Recently, we improved the performance of the MLAA algorithm using an MRI-constrained Gaussian mixture model (GMM). In this study, we compare the performance of our proposed algorithm with standard 4-class MR-based attenuation correction (MRAC) implemented on commercial systems. **Methods:** Five head and neck ^{18}F-FDG patients were scanned on the Philips TF PET/MRI and Siemens mCT PET/CT scanners. Dixon fat and water MR images were registered to CT images. MRAC maps were derived by segmenting the MRI into 4 tissue classes and assigning predefined attenuation coefficients. For MLAA-GMM, MR images were segmented into known tissue classes, including fat, soft tissue, lung, background air and an unknown MR low-intensity class encompassing cortical bones, air cavities and metal artifacts. A co-registered bone probability map was also included in the unknown tissue class. Finally, the GMM prior was constrained over known tissue classes of attenuation maps using uni-modal Gaussians parameterized over a patient population. **Results:** The results showed that the MLAA-GMM algorithm outperforms the MRAC method by differentiating bones from air gaps and providing more accurate patient-specific attenuation coefficients of soft tissue and lungs. It was found that the MRAC and MLAA-GMM methods resulted in average SUV errors of –5.4 % and –3.5 % in the lungs, –7.4 % and –5.0% in soft tissues/lesions, –18.4% and –10.2% in bones, respectively. **Conclusion**: The proposed MLAA algorithm is promising for accurate derivation of attenuation maps on TOF PET/MR systems.

Key Words: PET/MRI, time-of-flight, attenuation correction, quantification, whole-body imaging.

INTRODUCTION

Hybrid positron emission tomography/magnetic resonance imaging (PET/MRI) systems have provided new opportunities for enhancing the diagnostic confidence of PET and MRI findings through fusion of complementary structural and molecular information *(1)*. The potential of PET/MRI in establishing a new multi-parametric imaging paradigm has been a driving force for developing innovative solutions to tackle the challenges of these dual-modality systems.

Accurate attenuation correction (AC) of PET data is one of the major challenges of quantitative PET/MRI imaging *(2)*. In these systems, attenuation maps at 511 keV should ideally be derived from the acquired MR images. However, in contrary to x-ray computed tomography (CT), MRI signals are not correlated with electron density and photon attenuating properties of tissues, but rather to proton density and magnetic relaxation properties. Therefore, there is no unique global mapping technique to convert MRI intensities to attenuation coefficients. In addition, lung tissues and cortical bones, which are two important tissue types in attenuation maps, exhibit low signals on images acquired using conventional MR pulse sequences owing to their low water content and short transverse relaxation time. Therefore, the lungs, bones and air pockets, which also produce a low signal, cannot be well differentiated from each other for the generation of MRI segmentation-based attenuation maps. Ultra-short echo time (UTE) and zero echo time (ZTE) MR pulse sequences have been investigated for the detection and visualization of bones as well as lung parenchyma (*3-5*). However, UTE/ZTE MRI is timing-consuming and sensitive to magnetic field inhomogeneities and, as such, it is not yet clinically feasible for whole-body MRI-guided attenuation correction (MRAC) of PET data. Current commercial PET/MRI systems employ MRI segmentation-based approaches as the standard AC method. In these methods, MR images are segmented into 3 or 4 tissue classes, that is, background air, lung, fat and non-fat soft tissues, and predefined constant attenuation coefficients are assigned to each tissue class (*6,7*). However, inter/intra-patient heterogeneity of attenuation coefficients in the different tissue classes is ignored by these approaches. Moreover, since bones and air cavities cannot be well discriminated in conventional MR sequences, these tissue classes are often replaced by soft tissue, which can lead to significant bias in PET tracer uptake quantification in different organs (*8,9*). Hence, other AC techniques based on atlas registration, external transmission sources and PET emission data have been explored and revisited in PET/MRI imaging.

In atlas registration-based approaches, co-registered MR-CT atlas datasets are used to derive a pseudo CT image from the patient's MR image or to learn a mapping function that predicts a pseudo CT image (*10,11*). These methods can solve the MRAC problem, particularly in brain imaging, provided that a perfect registration between the atlas and different patients can be achieved. However, such a registration is rarely possible in whole-body PET/MRI, owing to substantial anatomical differences between patients as well as the limitations of registration algorithms. With advances in PET detector technology, time-of-flight (TOF) PET capability has been recently introduced in clinical PET/CT and PET/MRI scanners with the aim of improving lesion detectability and image quality, as well as reducing acquisition time and the administrated activity of radiopharmaceuticals (*12*). Following the recent rebirth of TOF-PET, transmission- and emission-based methods have been revisited for deriving patient-specific attenuation maps in PET/MRI, thus potentially circumventing the uncertainties and obstacles of both standard and UTE/ZTE MRAC methods. In transmission-based approaches, attenuation coefficients are directly measured using external

positron-emitting sources (*13*) or background radiation of LSO crystals (*14*) in a simultaneous transmission and emission acquisition mode. TOF information is then used to separate transmission from emission data. The limited timing resolution of current TOF PET scanners; however, does not allow for perfect separation of transmission data from emission data. Therefore, the calculated attenuation coefficients might be non-uniformly scaled and different from their expected values (*13*). In contrast, emission-based approaches only rely on emission data for joint maximum likelihood estimation of activity and attenuation maps (MLAA) (*15,16*). In fact, recent studies have demonstrated that both activity and attenuation distributions can be determined from TOF emission data, up to an unknown scaling factor (*16,17*).

Emission-based AC methods are promising in TOF PET/MRI, where MRI anatomical information can be exploited to guide the estimation of the attenuation map. With the advent of sequential TOF PET/MRI systems, Salomon *et al.* (*18*) employed both TOF and MRI anatomical information to constrain the MLAA algorithm. In their approach, MR images are segmented into many regions over which the attenuation coefficients are iteratively estimated from the emission data. Despite the fact that this approach substantially reduces noise and cross-talk artifacts between activity and attenuation maps, the reconstructed attenuation maps suffer from mis-segmentation errors and the quantitative performance of the algorithm depends on the accurate correction of the scaling problem. We recently proposed an approach to employ MRI spatial and CT statistical information in the joint estimation of activity and attenuation using a constrained Gaussian mixture model (GMM) (*19*). In contrast to Salomon's method, MR images are segmented into a few tissue classes and incorporated into the GMM model. This approach allows the derivation of continuous attenuation maps with noise suppression, cross-talk and the scale problem. In this work, we evaluated the performance of the proposed MLAA-GMM algorithm with standard 4-class MRAC over a patient population and demonstrated the potential advantage of MRI-guided emission-based AC methods over conventional MRI-guided segmentation based approaches.

MATERIAL AND METHODS

PET/MRI and PET/CT clinical data acquisition

In this retrospective clinical study, five patients with head and neck carcinoma were scanned on the Philips Ingenuity TF PET/MRI and the Siemens Biograph mCT flow PET/CT scanners as part of clinical workup. The average age and body mass index of patients were 57 ± 5 years and 24.6 ± 5.1 kg/m^2, respectively. The patients were injected with an average of 271 ± 9.3 MBq of ^{18}F-FDG and following a standard uptake time of 60 minutes during which various MR sequences are acquired, underwent a whole-body PET/MRI scan with arms-down position. After an interval of 10-20 minutes, the patients underwent a complementary PET/CT imaging of 10-12 minutes also with arms-down position. MRI acquisition was performed on the Achieva 3T MRI subsystem of the PET/MRI scanner. A whole-body scan was acquired in shallow breathing mode using a 3D multi-echo FFE Dixon technique using the following parameters: TR = 5.7 ms, TE1/TE2 = 1.45/2.6, flip angle = 10º and slice thickness of 3 mm, matrix size of 680 × 680. PET/CT scanning was performed in continuous bed motion mode with bed speed of 1.1 mm/sec, equivalent to 3 minutes per bed position in step and shoot mode. For CT-based attenuation correction (CTAC) of PET data, a multi-

slice CT scan protocol was performed using the following parameters: 100-120 kVp, 150 mAs and 5 mm slice thickness. Supplemental Figure 1 shows a flowchart of acquisition protocol used in this study. The TOF PET data of the mCT scanner was used for joint reconstruction of activity and attenuation maps and the anatomical MR images acquired on the Ingenuity PET/MRI scanner were used for MRI-guided MLAA and 4-class MRAC methods. In-phase (IP) MR images were deformably registered to CT images using the Elastix software (*20*), with 5-level multi resolution registration and Mattes mutual information criterion. The resulting transformation fields were then used for registration of fat and water images.

Attenuation map generation

MRI-guided emission-based attenuation map

In the framework of the maximum likelihood estimation, the MLAA algorithm jointly estimates activity (λ) and attenuation (μ) maps by maximization of the Poisson log-likelihood of time-of-flight PET emission data, i.e.

$$(\hat{\lambda},\hat{\mu}) = \underset{\lambda\geq 0,\mu\geq 0}{\operatorname{argmax}}\left\{\sum_{it} g_{it}\log\left(n_i a_i \sum_j c_{ijt}\lambda_j + \bar{b}_{it}\right) - n_i a_i \sum_j c_{ijt}\lambda_j + \bar{b}_{it}\right\} \quad \text{Eq. 1}$$

where g_{it} is the number of prompt coincidences measured by the PET scanner along line-of-response (LOR) i in TOF bin t; $\bar{b}_{it}$ is the expected number of random and scattered coincidences; n_i is detector normalization factors; $a_i = \exp\left(-\sum_j l_{ij}\mu_j\right)$ is attenuation factors; c_{ijt} is the geometric probability detection of annihilation events emitted from voxel j along LOR i in TOF bin t and l_{ij} is the intersection length of LOR i with voxel j in millimeters. Since the activity and attenuation variables are coupled in Eq. (1), the MLAA algorithm follows an iterative alternating maximization approach (*16*). In this approach, the algorithm alternates between an emission and a transmission maximum likelihood image reconstruction problem, which are respectively solved by a TOF ordinary Poisson ordered subset expectation maximization (OSEM) algorithm and a non-TOF ordered subset maximum likelihood for transmission tomography (OS-MLTR) algorithm. In the proposed MLAA-GMM algorithm, we employed a transmission maximum-a-posteriori (MAP) image reconstruction for estimation of attenuation by exploiting a Markov random field smoothness function (R_{MRF}) and a mixture of Gaussians model (R_{GMM}), defined as follows:

$$R_{MRF}(\mu) = -\beta \sum_j \sum_{k\in N_j} \frac{\omega_{jk}}{2}\left(\mu_k - \mu_j\right)^2 \quad \text{Eq. 2}$$

$$R_{GMM}(\mu) = \gamma \sum_j \log\left\{\sum_{h=1}^{H} \frac{\rho_h}{\sqrt{2\pi}\sigma_h}\exp\left(-\frac{1}{2}\left(\frac{\mu_j - \bar{\mu}_h}{\sigma_h}\right)^2\right)\right\} \quad \text{Eq. 3}$$

R_{MRF} favors attenuation maps that are smooth based on the weighted (ω) differences between voxel j and its neighboring voxels in the neighborhood N_j. R_{GMM} models the statistical distribution (histogram) of linear attenuation coefficients (LACs) in attenuation maps at 511-keV as a mixture of H known Gaussian functions with mean $\bar{\mu}_h$, standard deviation σ_h and mixture proportion ρ_h (*21*). The parameters β and γ weight the impact of the penalty functions. In the proposed MLAA-GMM algorithm, the R_{GMM} is iteratively approximated using a convex surrogate and spatially constrained by MRI anatomical information using a tissue prior map. This prior map contains known and unknown tissue classes, over which uni-modal Gaussians and a mixture of Gaussians are respectively imposed

on the estimation of LACs during OS-MLTR algorithm. Figure 1 presents the flowchart of the proposed MLAA-GMM algorithm. In this work, the algorithm was initialized by a uniform activity map and a 4-class MRAC map.

For generation of the tissue prior map (Figure 2), Dixon water and fat MR images are segmented into 4 known tissue classes including fat, soft tissue, lungs and background air, and an additional unknown tissue class corresponding to the regions with low MR intensity (i.e. cortical bones, air pockets and metal induced susceptibility artifacts). Due to partial volume averaging and incomplete Dixon water and fat separation, spongy bones might possess moderate MR intensities in water images and therefore be classified as known soft and fat tissue classes instead of the unknown class. To eliminate this misclassification, we subtracted the fat from water images and used a bone probability map, obtained from a co-registered average CT, to insure the inclusion of bones into the unknown class. The soft-tissue class was segmented by thresholding the fat-suppressed water images. The fat class was defined based on the voxels of the fat image whose intensities are 50% larger than the water image. The lungs and background air were segmented from IP MR images using a supervised seeded region-growing method implemented in the ITK-SNAP software (*22*). In the proposed MLAA method, a mixture of 4 Gaussians representing inside air, fat/soft mixture and bone was used to guide the attenuation estimation over the unknown tissue class. The parameters of the mixture model and uni-modal Gaussians were estimated from 10 whole-body CTAC maps (*19*). Supplemental Figure 2 presents the estimated parameters.

MRI-guided segmentation-based attenuation map

Standard 4-class MRAC maps were derived by segmenting the Dixon water and fat images into 4 tissue classes: background air, lung, fat, and non-fat soft tissues. The background air, lungs and fat tissue classes were obtained with the same procedure used for deriving the tissue prior map. The non-fat soft tissue class was then defined as the complement of the segmented classes. In this procedure, all bones, air pockets and susceptibility artifacts are assigned to the non-fat soft tissue class. Mean attenuation coefficients of 0, 0.0224, 0.0864 and 0.0975 cm^{-1} were assigned to background air, lungs, fat and non-fat soft tissue classes, respectively. The CT bed attenuation map was also added to the resulting MRAC maps.

CT-based attenuation map

For comparison of the MLAA and MRAC methods against a reference attenuation correction method, CT-based attenuation maps were generated for each patient using Siemens e7 tools. High-resolution CT images were down-sampled to a resolution of 400×400. CT Hounsfield units were then converted to 511 keV attenuation values using a kVp-dependent bilinear mapping approach. The resulting maps were finally smoothed to the resolution of PET images using 4-mm FWHM isotropic Gaussian filtering.

PET image reconstruction

TOF PET data acquired on the mCT PET/CT scanner were reconstructed using a 3D time-of-flight OSEM algorithm with 3 different AC methods: MRI-guided emission-based, MR-guided segmentation-based and CT-based. PET images were reconstructed with 3 iterations and 21 subsets and a matrix size of 200×200 with 4×4×2 mm^3 voxels. For the MLAA-GMM algorithm, an in-house software was developed for the native geometry of the mCT scanner with the following specifications: 400 radial bins, 168 azimuthal angles, 621 planes and13 TOF bins. The

coincidence window width and effective TOF resolution of the scanner are 4.1 and 0.58 ns, respectively. The activity and attenuation maps were reconstructed with 1 iteration and 2 subsets of the OSEM algorithm and 1 iteration and 3 subsets of the OS-MLTR algorithm with 20 global iterations. As mentioned above, the algorithm was initialized with a 4-class MRAC map with a TOF scatter simulated using the same MRAC map. Based on our previous work (*19*), the β and γ parameters (in Eqs. 2 and 3) were experimentally set to 80 and 0.015, respectively. The estimated attenuation maps were then used for a standard OSEM PET image reconstruction.

Quantitative evaluation

The relative quantification error (bias) in the standardized tracer uptake (SUV) was calculated on a volume of interest (VOI) basis for each patient with respect to the reference CTAC-PET as follows:

$$Bias = 100 \times \frac{SUV_m - SUV_{CTAC}}{SUV_{CTAC}} \qquad \text{Eq. 4}$$

where m is the attenuation correction method used (MLAA or MRAC). For each patient, 14 VOIs were defined on normal tissue regions including the lungs (upper, middle and lower portions of left and right lungs), aorta, liver, myocardium, thyroid, cerebrum, 4th cervical (C4), 3rd thoracic (T3) and 4th lumbar (L4) vertebra. VOIs were also defined on lesions localized on CTAC-PET images. For the defined VOIs, the mean (μ), standard deviation (σ) and root-mean-squared error (RMSE) of bias ($\sqrt{\mu^2 + \sigma^2}$) was calculated. The correlation between SUV_{MRAC} and SUV_{MLAA} and reference SUV_{CTAC} was determined using Pearson correlation analysis. The concordance between the SUVs was evaluated using Bland-Altman plots. The statistical differences in SUV bias was also calculated using the paired-sample *t*-test. The differences were considered statistically significant for $P < 0.05$.

RESULTS

Figure 3 compares the CTAC map of a representative patient with the attenuation maps obtained using the proposed MLAA-GMM algorithm and the 4-class MRAC method. As shown, the MLAA-GMM algorithm can reasonably well estimate the attenuation coefficients of bones and discriminate air cavities, particularly paranasal sinuses. In contrast, the bones and air gaps in the MRAC maps are simply replaced by soft tissue, which can lead to quantification errors in the reconstructed PET images. Figure 4 shows the close-up views of the attenuation maps over the lungs in different displaying windows. The CTAC map shows that the lungs of this patient have a congested structure especially in the left lung. As indicated by the arrows, some of the condensed soft tissue structures in the MRAC map have been erroneously segmented into lung tissue class, whereas the MLAA-GMM algorithm compensates for the mis-segmentation of these structures and also retrieves lung density gradients. Note that because of respiratory motion of the lungs during PET acquisition and count-dependent performance of the MLAA algorithm, the estimated attenuation coefficients cannot preserve all local details. For this dataset, the lung attenuation coefficients of the CTAC, MLAA and MRAC attenuation maps, filtered by a 4-mm FWHM Gaussian filter, were 0.0293 ± 0.0077, 0.0301 ± 0.0075, 0.0225 ± 0.0003 cm^{-1}, respectively. Supplemental Figure 3 compares the attenuation maps of another patient study, where the MLAA-GMM algorithm also compensates for a mis-segmented pathology and accurately retrieves the lung density gradient in a continuous fashion. Figure 5 shows

activity and attenuation maps of another study in which the MLAA algorithm also compensated for respiratory phase-mismatch between activity and attenuation maps. As pointed by the arrow, the uptake at the upper lobe of the liver has been underestimated by CTAC and MRAC methods due to under-correction of attenuation. As shown on the attenuation maps and profiles, the MLAA algorithm estimates correctly the underlying attenuation experienced by the emission data and therefore increases liver uptake, thus improving the detection and quantification of possible upper-lope lesions.

Table 1 compares the mean ± standard deviation of linear attenuation coefficients of different tissue classes of the CTAC, MLAA and MRAC attenuation maps calculated over all patient datasets. For these class-wise calculations, the lung, fat and soft tissue classes were obtained from the tissue prior map built for each patient (see Figure 2). The bone class was derived by thresholding CTAC images at 0.109 cm^{-1}. As can be seen, the main difference between MLAA and MRAC methods sits over the lungs and bones, for which the maximum PET quantification errors occurs when using standard MRAC methods. The results show that the MLAA-GMM algorithm outperforms the MRAC method over these tissue classes by estimating mean and standard deviation of LACs which are closer to those of the reference CTAC method. The proposed method, however, slightly over- and under-estimates the mean of the LACs of lungs and bones. In fat and soft tissue classes, both MLAA and MRAC attenuation maps have a similar mean as the CTAC maps, while the standard deviations of only MLAA's LACs are close to those of CTAC maps.

The quantitative PET performance of MRI-guided attenuation correction methods was further evaluated in comparison with the CTAC method using VOI-based analysis. Table 2 summarizes the mean, standard deviation and root-mean-squared error of SUV_{mean} bias in VOIs defined in normal tissue and lesions. Figure 6(A) shows the errors in each VOI, grouped for the lung and soft tissue organs, while Figure 6(B) shows the results for VOIs defined on bones or soft tissues located close to bones. In this figure, the markers show the mean of bias in each VOI, while the horizontal bars and vertical boxes indicate the mean and two-standard deviations of the bias between VOIs in each region. The results show that the MLAA-GMM algorithm generally gives rise to a reduced RMSE bias over all regions. For VOIs defined in the lungs (n = 30), the MRAC method underestimates SUV_{mean} by –5.4 ± 12.0 % with a RMSE of 13.1%, while MLAA-GMM reduces the errors to –3.5 ± 6.6 % with a RMSE of 7.5%. For the total VOIs defined on the aorta, myocardium, liver and thyroid (n = 20), MRAC and MLAA-GMM methods resulted in average SUV errors of –7.0 ± 6.6% (9.6% RMSE) and –4.9 ± 5.5% (7.4% RMSE), respectively. Over the lesions (n = 11), which were mainly mediastinal lymphoma, the MLAA-GMM reduced the errors from –9.0 ± 5.4% with RMSE of 10.5% to –4.5 ± 5.3% with RMSE of 7.0%. Finally, for all regions in or near bones (n = 20), the MRAC and MLAA algorithms resulted in an average SUV error of –18.4 ± 7.9% (20.0% RMSE) and –10.2 ± 6.5% (12.1% RMSE), respectively. The statistical analysis revealed that there is an overall significant difference (P <0.05) between the proposed MLAA-GMM and MRAC methods in bones, malignant lesions and most soft tissue regions. The results also showed that the bias differences in the lungs are insignificant.

The SUV correlation and concordance of the MLAA and MRAC methods with reference CTAC was further evaluated. Figure 7 (top panel) shows the scatter plots of the SUV_{mean} in all studied VOIs between PET-CTAC, PET-MRAC and PET-MLAA with correlation and regression coefficients. The results show that PET-MLAA and PET-MRAC are highly correlated with PET-CTAC with R^2 values of 0.982 and 0.992, respectively. Figure 7 (bottom panel) shows the results of Bland-Altman concordance analysis. The limits of agreement (LA) were calculated from

logarithmically transformed values. Differences and LA are expressed as a function of average SUVs. As shown by the regression lines of the difference, MRAC and MLAA attenuation correction methods result in a systematic underestimation of SUV by up to 9.85% and 6.75%, respectively. However, MLAA clearly outperforms MRAC by reducing the errors and their dispersion.

DISCUSSION

Interest in the estimation of PET attenuation maps from emission data has recently been revived in the context of TOF PET/MRI attenuation correction to overcome the limitations and quantification errors of standard segmentation-based MRAC methods (*18,19*). In this work, we compared the performance of our previously reported MLAA algorithm with the standard MRAC method to demonstrate the potential of emission-based AC methods in TOF PET/MRI imaging.

In segmentation-based MRAC methods, the mis-segmentation of the lungs and the assignment of non patient-specific lung attenuation coefficients can result in PET quantification errors. Our results demonstrated that, consistent with previously reported results (*23*), the MRAC method results in errors in the lungs of up to 26% (Figure 6). Due to their low proton density and short T_2* relaxation time, the lungs show low signal intensity in the fast gradient-recalled echo (GRE) pulse sequences conventionally used in whole-body MRI acquisitions. Therefore, in conjunction with the limitations of segmentation-based MRAC algorithms, the soft tissue structures of the lungs, for example, pulmonary vessels and bronchioles, might be miss-segmented into lung class. Our results showed that the MLAA-GMM algorithm not only fairly compensates for the mis-segmentations but also derives more patient-specific lung LACs (Figure 4 and Supplemental Figure 3). Hence, as reported in Table 2, the RMSE in the lungs was reduced from 13.1% to 7.5%. In contrary to Salomon *et al* (*18*), our proposed MLAA estimates continuous attenuation coefficients and thus retrieves the lung density gradients and intra-patient variability of lung attenuation coefficients. Continuous lung LACs can also be derived from atlas-registration-based AC methods. However, these approaches had a limited success owing to the low signal of the lungs (*10*).

Another limitation of segmentation-based MRAC is that the identification of bones, which produce low signal intensity in GRE MRI pulse sequences, is very challenging. In 4-class MRAC maps, the bones are replaced by soft tissue, which based on our results can lead to a mean bias of –18.4%, which is consistent with the >15% errors reported previously (*9,23*). As demonstrated in this work, the proposed MLAA-GMM algorithm is capable of estimating bone attenuation coefficients, thus outperforming the MRAC method by reducing the mean error to –10.2%. Bezrukov *et al.* reported that a combination of segmentation and atlas-registration based AC methods can effectively reduce bone SUV errors of the 4-class MRAC from –16.1% to –4.7% (*8*). However, the performance of these techniques depends on accurate atlas registration and robust prediction of attenuation coefficients. In contrast, several CT images are registered to patient's IP MR image in our MRI-constrained MLAA algorithm to only roughly indicate the position of the bones. Therefore, this technique is in principle not subjected to mis-registration errors.

As indicated in Supplemental Figure 2, we set the means of Gaussian models defined in known tissue classes to the mean LACs used in the 4-class MRAC maps. Therefore, for very high values of the γ parameter in Eq. 3, the MLAA-GMM is essentially reduced to a 4-class MRAC method. The results show that the MLAA and MRAC

methods present similar mean LACs in fat and soft tissue classes (Table 1); however, only for MLAA the standard deviation (inter/intra-variability) of LACs are similar to the reference CTAC method. Combined with more accurate derivation of lung and bone LACs, our MLAA-GMM approach resulted in improved quantitative performance over soft tissue organs compared with the MRAC method (Table 2).

The results of this feasibility study demonstrate the potential of the emission-based AC methods for accurate attenuation correction in TOF PET/MRI. However, it is worth highlighting the limitations of the proposed algorithm and the study conducted herein. Similar to other MAP reconstruction techniques, the performance of the MLAA-GMM depends on the selection of the regularization parameters, especially the γ parameter of the GMM model. In this work, we set the γ and the β parameter in Eq. 2 to experimentally optimized values for a few simulation and clinical studies (*19*). In general, the MLAA algorithm is time consuming since it alternates between an emission and transmission tomographic reconstruction. The preparation of a tissue prior map can further increase the computational burden of the proposed MLAA-GMM method. In this first clinical study, a relatively small number of PET/MR/CT datasets could be included. Therefore, the statistical significance of our results might be subject to a degree of uncertainty. Future work will focus on further evaluation of the studied AC methods using a large clinical patient database acquired with different tracers to pave the way for translation of emission-based AC methods into the clinic.

CONCLUSION

In this work, the performance of an MRI-guided emission-based AC method was compared with the standard segmentation-based MRAC method using clinical studies. It was demonstrated that the proposed constrained MLAA algorithm is promising for deriving patient-specific attenuation maps, especially in the lungs and bones. Our results showed that the MRAC method resulted in average SUV errors of –5% and –18% in the lungs and bones, while the proposed algorithm reduced the errors to –3% and –10%, respectively. It can be concluded that emission-based attenuation correction is promising in clinical TOF PET/MRI imaging and presents the potential to replace conventional segmentation-based methods implemented on commercial systems.

DISCLOSURE

The authors declare no conflict of interest.

ACKNOWLEDGMENTS

This work was supported in part by the Swiss National Science Foundation under Grant SNSF 31003A-149957 and the Indo-Swiss Joint Research Programme ISJRP-138866

References

1. Torigian DA, Zaidi H, Kwee TC, et al. PET/MR Imaging: Technical aspects and potential clinical applications. *Radiology* 2013; 267:26-44.
2. Bezrukov I, Mantlik F, Schmidt H, Scholkopf B, Pichler BJ. MR-Based PET attenuation correction for PET/MR imaging. *Semin Nucl Med* 2013; 43:45-59.
3. Keereman V, Fierens Y, Broux T, De Deene Y, Lonneux M, Vandenberghe S. MRI-based attenuation correction for PET/MRI using ultrashort echo time sequences. *J Nucl Med* 2010; 51:812-8.
4. Zeimpekis K, Delso G, Wiesinger F, Veit-Haibach P, von Schulthess G, Grimm R. Investigation of 3D UTE MRI for lung PET attenuation correction. *J Nucl Med* 2014; 55:2103.
5. Delso G, Wiesinger F, Sacolick LI, et al. Clinical evaluation of Zero-Echo-Time MR imaging for the segmentation of the skull. *J Nucl Med* 2015; 56:417-422.
6. Martinez-Möller A, Souvatzoglou M, Delso G, et al. Tissue classification as a potential approach for attenuation correction in whole-body PET/MRI: evaluation with PET/CT data. *J Nucl Med* 2009; 50:520-526.
7. Zaidi H, Ojha N, Morich M, et al. Design and performance evaluation of a whole-body Ingenuity TF PET-MRI system. *Phys Med Biol* 2011; 56:3091-3106.
8. Bezrukov I, Schmidt H, Mantlik F, et al. MR-based attenuation correction methods for improved PET quantification in lesions within bone and susceptibility artifact regions. *J Nucl Med* 2013; 54:1768-1774.
9. Arabi H, Rager O, Alem A, Varoquaux A, Becker M, Zaidi H. Clinical assessment of MR-guided 3-class and 4-class attenuation correction in PET/MR. *Mol Imaging Biol* 2015; *in press*
10. Hofmann M, Steinke F, Scheel V, et al. MRI-based attenuation correction for PET/MRI: a novel approach combining pattern recognition and atlas registration. *J Nucl Med* 2008; 49:1875-1883.
11. Navalpakkam BK, Braun H, Kuwert T, Quick HH. Magnetic resonance-based attenuation correction for PET/MR hybrid imaging using continuous valued attenuation maps. *Invest Radiol* 2013; 48:323-32.
12. Surti S. Update on Time-of-Flight PET Imaging. *J Nucl Med* 2015; 56:98-105.
13. Mollet P, Keereman V, Bini J, Izquierdo-Garcia D, Fayad ZA, Vandenberghe S. Improvement of attenuation correction in time-of-flight PET/MR imaging with a positron-emitting source. *J Nucl Med* 2014; 55:329-36.
14. Rothfuss H, Panin V, Moor A, et al. LSO background radiation as a transmission source using time of flight. *Phys Med Biol* 2014; 59:5483-500.
15. Nuyts J, Dupont P, Stroobants S, Benninck R, Mortelmans L, Suetens P. Simultaneous maximum a posteriori reconstruction of attenuation and activity distributions from emission sinograms. *IEEE Trans Med Imaging* 1999; 18:393-403.
16. Rezaei A, Defrise M, Bal G, et al. Simultaneous reconstruction of activity and attenuation in time-of-flight PET. *IEEE Trans Med Imaging* 2012; 31:2224-33.
17. Defrise M, Rezaei A, Nuyts J. Time-of-flight PET data determine the attenuation sinogram up to a constant. *Phys Med Biol* 2012; 57:885-899.
18. Salomon A, Goedicke A, Schweizer B, Aach T, Schulz V. Simultaneous reconstruction of activity and attenuation for PET/MR. *IEEE Trans Med Imaging* 2011; 30:804-813.

19. Mehranian A, Zaidi H. Joint estimation of activity and attenuation in whole-body TOF PET/MRI using constrained Gaussian mixture models. *IEEE Trans Med Imaging* 2015; *in press*
20. Klein S, Staring M, Murphy K, Viergever MA, Pluim JP. Elastix: a toolbox for intensity-based medical image registration. *IEEE Trans Med Imaging* 2010; 29:196-205.
21. Anderson JMM, Yoon-Chul K, Votaw JT. Concurrent segmentation and estimation of transmission images for attenuation correction in positron emission tomography. *IEEE Trans Nuc Sci* 2009; 56:136-146.
22. Yushkevich PA, Piven J, Hazlett HC, et al. User-guided 3D active contour segmentation of anatomical structures: significantly improved efficiency and reliability. *Neuroimage* 2006; 31:1116-28.
23. Keereman V, Holen RV, Mollet P, Vandenberghe S. The effect of errors in segmented attenuation maps on PET quantification. *Med Phys* 2011; 38:6010-9.

Table 1. Mean ± standard deviation of LACs of different tissue classes of CTAC, MLAA and MRAC attenuation maps calculated over all clinical studies.

	Lung	**Fat**	**Soft tissue**	**Bone**
CTAC	0.025 ± 0.009	0.087 ± 0.009	0.098 ± 0.008	0.118 ± 0.012
MLAA	0.027 ± 0.008	0.086 ± 0.010	0.097 ± 0.006	0.104 ± 0.012
MRAC	0.022 ± 0.001	0.086 ± 0.004	0.097 ± 0.001	0.095 ± 0.005

Table 2. Quantification bias [Mean ± SD, (RMSE)%] of PET-MRAC and PET-MLAA in different tissues with respect to reference PET-CTAC.

VOI	MRAC	MLAA	*P*-value
Lung	–5.4 ± 12.0 (13.1)	–3.5 ± 6.6 (7.5)	0.1605
Aorta	–9.5 ± 10.5 (14.1)	–7.6 ± 9.3 (12.1)	0.0942
Liver	–7.4 ± 1.8 (7.6)	–5.4 ± 3.2 (6.3)	0.0376
Myocardium	–9.2 ± 6.0 (11.0)	–3.1 ± 6.8 (7.5)	0.0027
Thyroid	–1.9 ± 8.8 (9.0)	–3.6 ± 5.1 (6.3)	0.6574
Lesions	–9.0 ± 5.4 (10.5)	–4.5 ± 5.3 (7.0)	0.0237
Cerebrum	–18.5 ± 11.3 (21.6)	–11.6 ± 6.0 (13.1)	0.0503
C4	–22.9 ± 2.7 (23.1)	–12.3 ± 3.1 (12.7)	0.0011
T3	–19.8 ± 8.4 (21.5)	–12.6 ± 8.6 (15.2)	<0.001
L4	–12.4 ± 4.5 (13.2)	–4.2 ± 4.4 (6.1)	<0.001

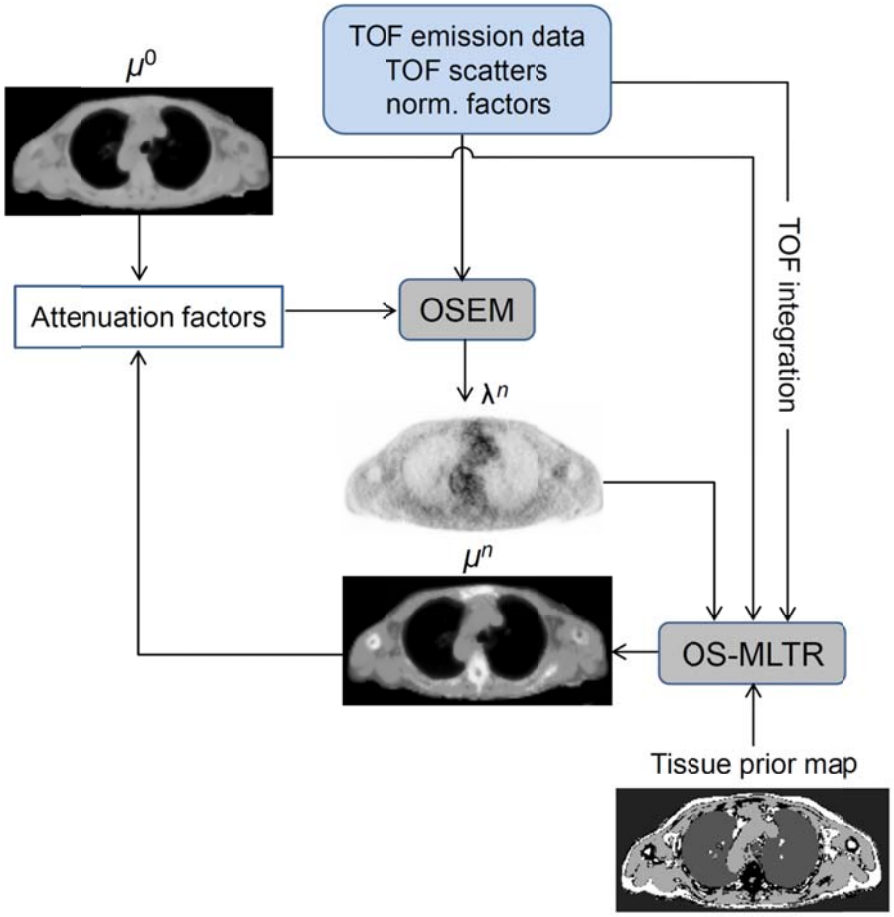

Figure 1. Flowchart of the MLAA-GMM algorithm, which alternates between an OSEM activity reconstruction and an OS-MLTR attenuation reconstruction. The algorithm is initialized by a 4-class MRAC attenuation map and MRI-based scatter sinograms. The GMM model is spatially constrained by the tissue prior map.

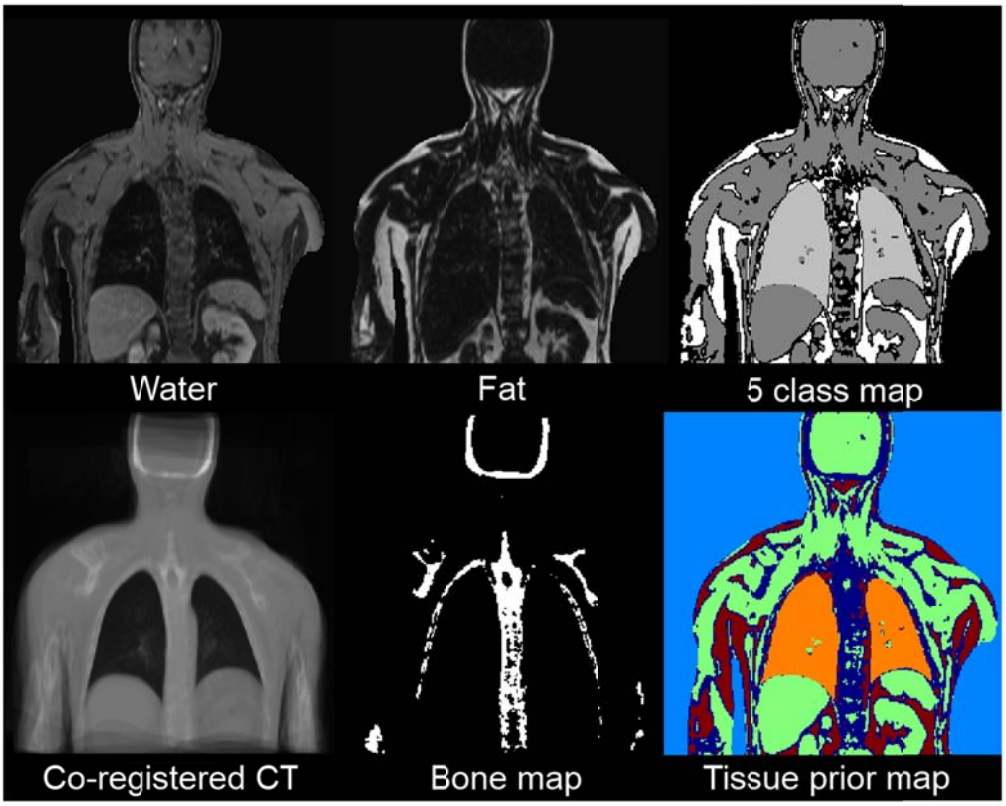

Figure 2. Derivation of the tissue prior map. Fat and water Dixon images are segmented into background air, fat, soft tissue, lungs and a low-intensity class (5-class). The possible position of bones is determined from a co-registered average CT image.

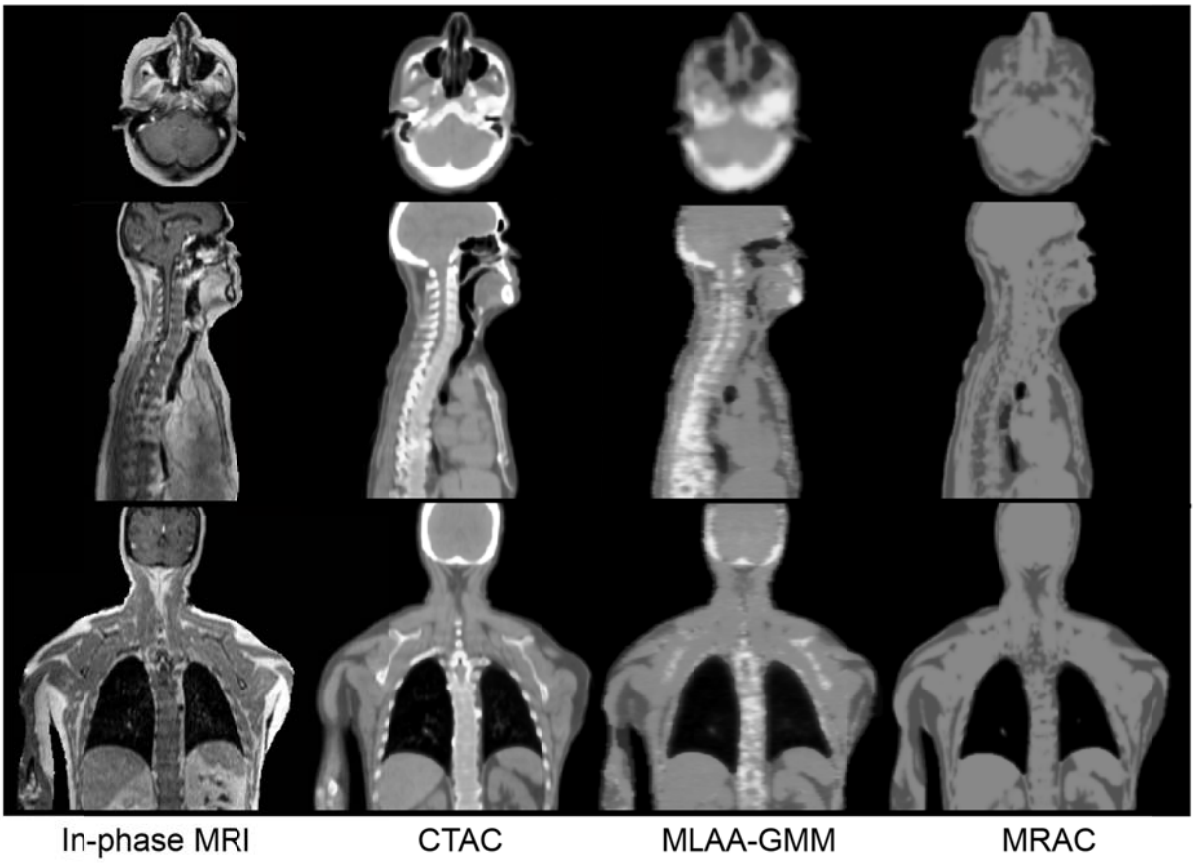

Figure 3. Comparison of 4-class MRAC and MLAA-GMM attenuation maps with their reference CTAC map from a representative ^{18}F-FDG PET/CT/MRI study. The display window is 0.08 ± 0.055 cm^{-1}.

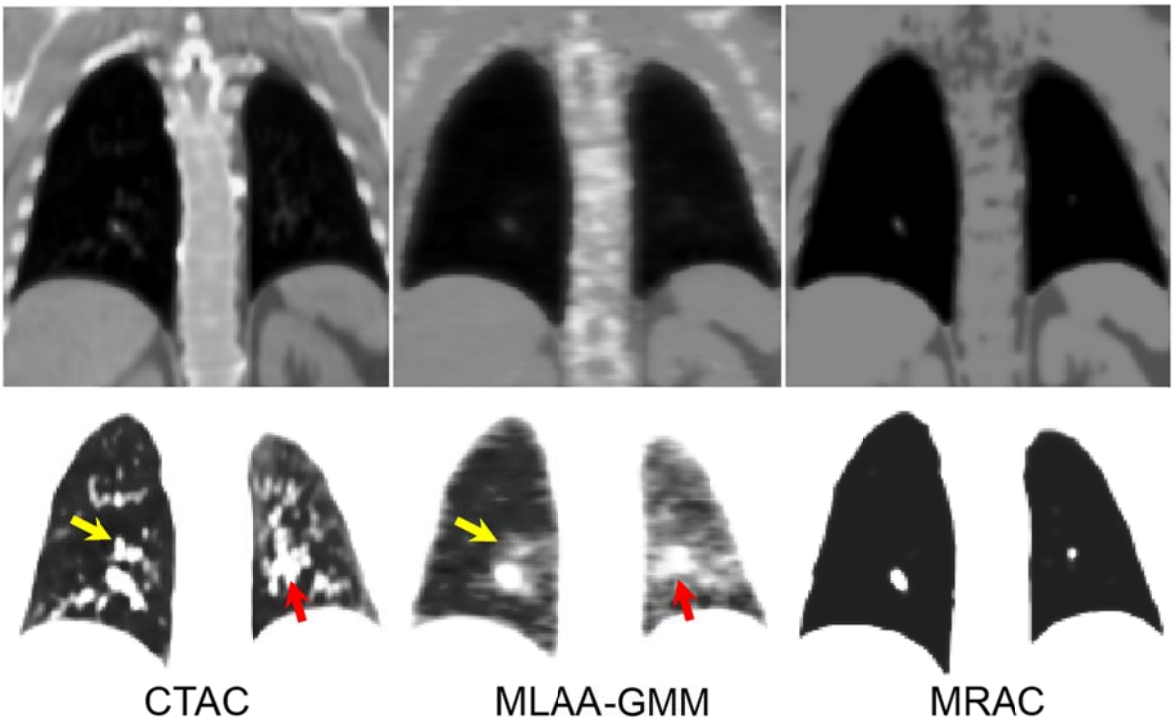

Figure 4. Close-up views of the lungs in different displaying windows. Top: 0.08 ± 0.055 cm^{-1}, bottom: 0.03 ± 0.03 cm^{-1}.

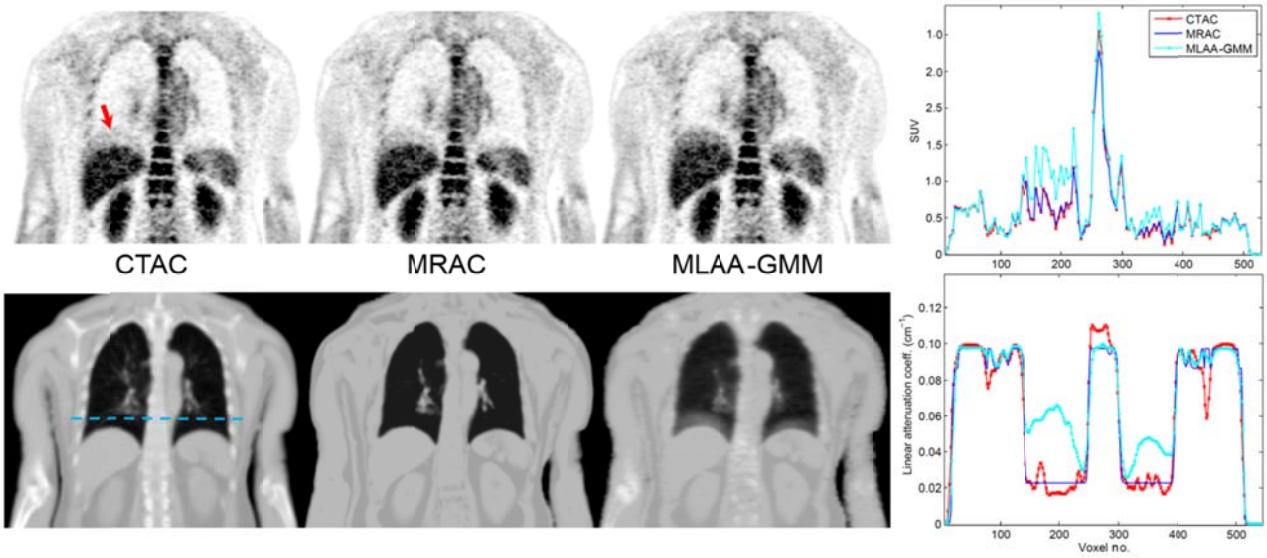

Figure 5. PET images and attenuation maps of a patient presenting with respiratory-phase mismatch between PET and CT/MRI acquisitions. The activity and attenuation profiles along the dashed line shown on the CTAC attenuation map are also shown.

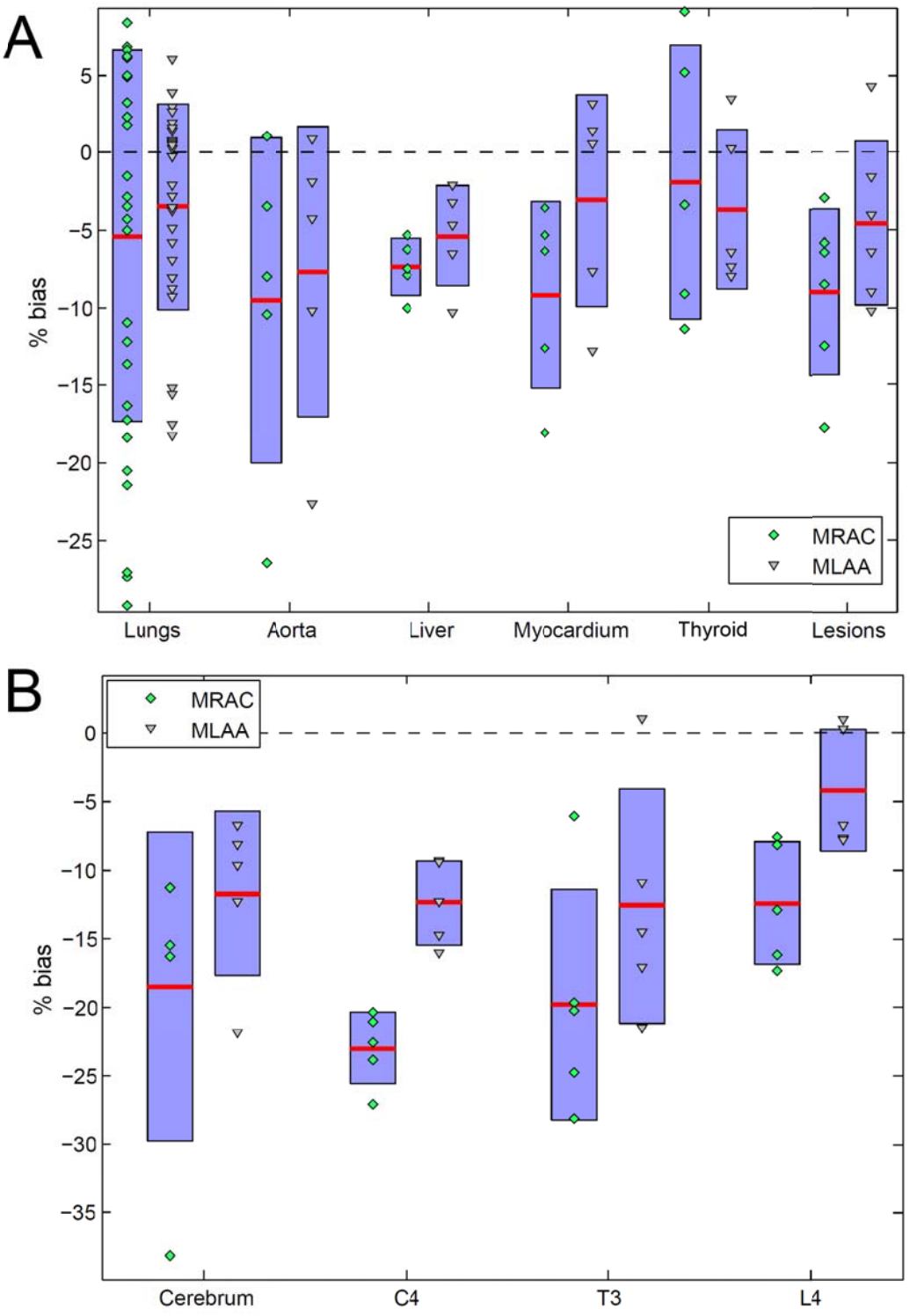

Figure 6. Mean SUV errors between PET-MRAC and PET-MLAA with respect to reference PET-CTAC images in VOIs defined on (A) normal tissues and lesions, and (B) in/near bones. Means and standard deviations are indicated by horizontal bars and vertical boxes, respectively. C4, T3 and L4 represent the 4th cervical, 3rd thoracic and 4th lumbar vertebra.

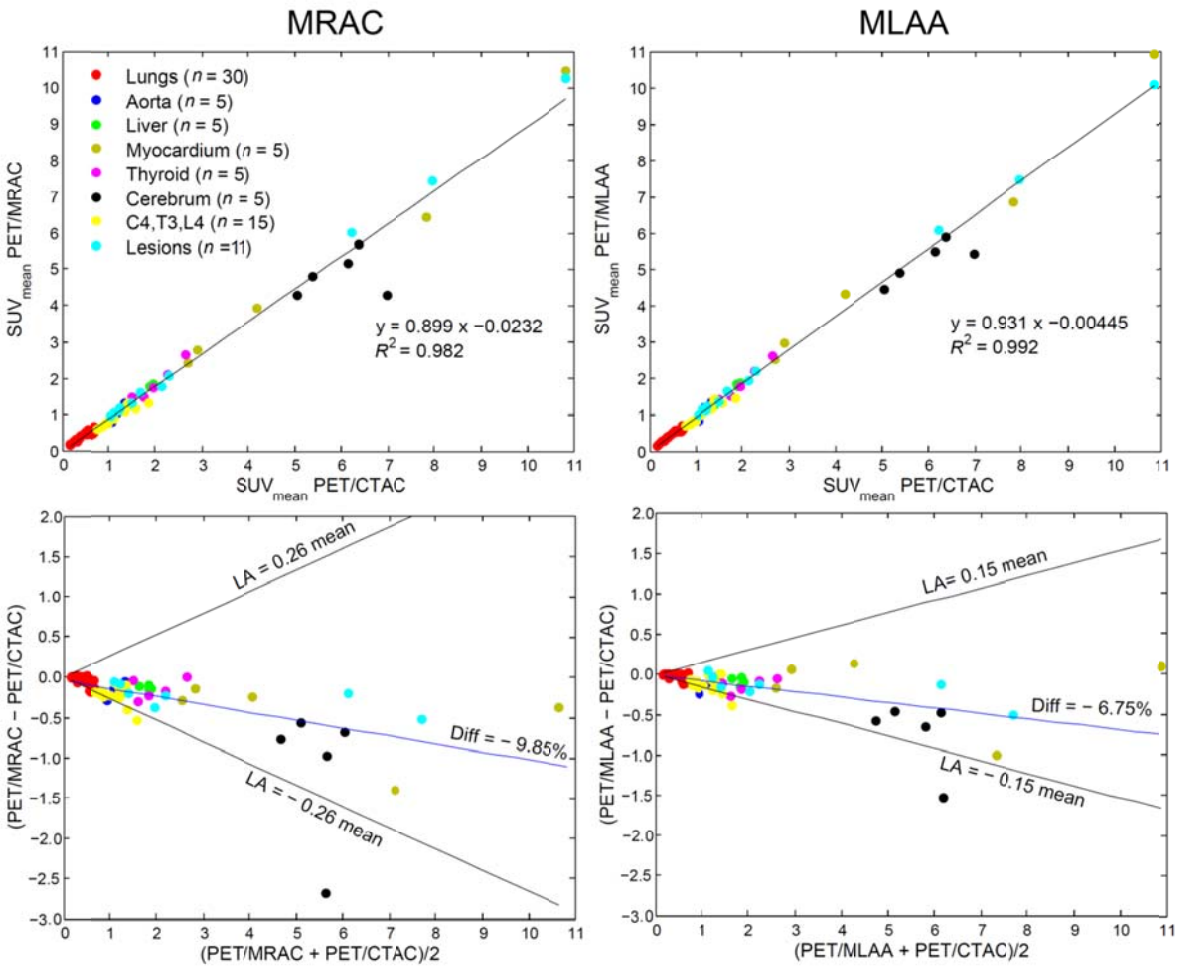

Figure 7. (Top) Scatter plots between the SUV_{mean} of PET images reconstructed using CTAC, MLAA-GMM and MRAC attenuation correction methods. (Bottom) SUV_{mean} Bland-Altman concordance plots.